In situ synchrotron diffraction of pressure-induced phase transition in math xmlns="http://www.w3.org/1998/Math/MathML">mrow>msub>mi>DyPO/mi>mn>4/mn>/msub>/mrow>/math> under variable hydrostaticity

Jai Sharma, Matthew Musselman, Bianca Haberl, and Corinne E. Packard

Phys. Rev. B **103**, 184105 — Published 12 May 2021

DOI: 10.1103/PhysRevB.103.184105

In situ synchrotron diffraction of pressure-induced phase transition in $DyPO_4$ under variable hydrostaticity

Jai Sharma[1], Matthew Musselman[1], Bianca Haberl[2], Corinne E. Packard[1*]

[1] *Colorado School of Mines, Golden, Colorado 80401, USA,* [2] *Neutron Scattering Division, Neutron Sciences Directorate, Oak Ridge National Laboratory, Oak Ridge, Tennessee 37831, USA.*

[*] *Correspondence e-mail: cpackard@mines.edu*

In situ synchrotron x-ray diffraction is conducted on polycrystalline $DyPO_4$ to elucidate the details of the pressure-induced transition from the xenotime polymorph to the monazite polymorph. We use three different pressure transmitting media (neon, a 16:3:1 methanol-ethanol-water mixture, and potassium chloride) to investigate the effect of hydrostaticity on the phase behavior. Specifically, our data clearly show a hydrostatic onset pressure of the xenotime-monazite transition of 9.1 GPa – considerably lower than the 15.3 GPa previously determined by Raman spectroscopy. Based on (quasi-)hydrostatic data taken in a neon environment, 3rd order Birch-Murnaghan equation-of-state fits give a xenotime bulk modulus of 144 GPa and a monazite bulk modulus of 180 GPa (both with pressure derivatives of 4). Structural data and axial compressibilities show that $DyPO_4$ is sensitive to shear and has an anisotropic response to pressure. More highly deviatoric conditions cause the onset of the transition to shift to pressures at least as low as 7.0 GPa. We attribute early transition to shear-induced distortion of the PO_4 tetrahedra. Our characterization of the high-pressure behavior of $DyPO_4$ under variable hydrostaticity is critical for advancing rare earth orthophosphate fiber coating applications in ceramic matrix composites and may inform future tailoring of phase composition for controlled shear and pressure applications.

PACS numbers: 61.50.Ks, 61.05.cp, 64.30.+t, 81.30.Hd

I. INTRODUCTION

Rare earth orthophosphates ($REPO_4$s) are a burgeoning class of ceramics, most of which transition to other phases under pressure [1-3]. In equilibrium at atmospheric pressure, heavier compositions (RE = Tb-Lu, Sc, Y) adopt the xenotime (tetragonal, $I4_1/amd$) structure while lighter compositions (RE = La-Gd) adopt the monazite (monoclinic, $P2_1/n$) structure [4]. At high pressures, xenotime compositions can transition into monazite or other structures. This polymorphism has spurred recent interest in $REPO_4$s for ceramic matrix composite (CMC) applications, where the xenotime-monazite transition offers the possibility of additional plasticity and toughening mechanisms in oxide-oxide CMCs [5,6]. In particular, Hay *et al.* showed that $DyPO_4$ (among other xenotime) fiber coatings deflect cracks and result in lower fiber push-out stresses than monazite $LaPO_4$ coatings.

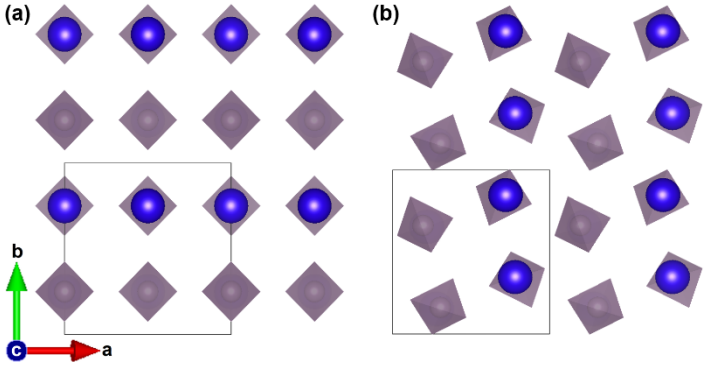

FIG. 1. (Color online) [001] views of the (a) xenotime and (b) monazite phases of dysprosium orthophosphate, $DyPO_4$. Violet spheres represent Dy^{3+} cations, grey tetrahedra represent PO_4^{3-} groups, and the boxes represent one unit cell. The apparent 90° rotation of monazite with respect to xenotime is merely a result of monazite's monoclinic cell setting.

Figure 1 shows the xenotime and monazite structures of $DyPO_4$ and the mechanism of transition is as follows: under compression, Dy-O bonds are distorted to the point of reconfiguration (the RE coordination number increases from 8 to 9), while the PO_4 groups (grey tetrahedra) are effectively rigid [7,8]. This description is widely accepted for all $REPO_4$ compositions that undergo the xenotime-monazite transition.

Most xenotime $REPO_4$ transitions have been extensively investigated using *in situ* diamond anvil cell (DAC) Raman spectroscopy (RS) and x-ray diffraction (XRD) techniques. For $TbPO_4$, Tatsi *et al.*'s RS study reported a high-pressure polymorph that was likely monazite [9]. López-Solano *et al.*'s XRD study then confirmed that this polymorph was of the monazite structure and

provided detailed structural information including an equation of state (EoS) for both polymorphs [10]. Gomis *et al.*'s single-crystal XRD work showed that $HoPO_4$ and $TmPO_4$ transition to the monazite structure and gave elastic constants and an EoS for each material in the xenotime phase [11]. Lacomba-Perales *et al.*'s synchrotron XRD study showed the xenotime-monazite transition in $ErPO_4$ and YPO_4 and gave an EoS for both polymorphs [3]. However, all xenotime compositions do not transition to monazite; Zhang *et al.* reported that $YbPO_4$, $LuPO_4$, and $ScPO_4$ transition to the scheelite (tetragonal, $I4_1/a$) structure [12,13].

Similar insight into the high-pressure phase behavior of $DyPO_4$ has yet to be reported, though significant steps have been taken. Using *in situ* DAC RS, Musselman *et al.* and Stavrou *et al.* reported $DyPO_4$ transition onset pressures (P_{onset}) of 15.3(9) GPa and 13 GPa, respectively [14,15]. They both attribute emergent Raman peaks at these pressures to a polymorph that takes on the monoclinic, monazite structure. Musselman et al.'s determination is based on peaks emerging at locations consistent with monazite $TbPO_4$ peaks. Stavrou et al. further claim that monazite $DyPO_4$ transforms to scheelite at higher pressures around 30 GPa. This xenotime-monazite-scheelite transition pathway is consistent with that of neighboring xenotime $REPO_4$s [15]. Other ABO_4 compounds like alkaline-earth phosphates are stable in the monazite structure up to at least 30 GPa [3]. Very recently, Heuser *et al.* synthesized metastable $DyPO_4$ in the monazite structure [16]. While literature on the xenotime and monazite $DyPO_4$ polymorphs exists, the fundamental thermodynamics and kinetics of the transition are not fully established.

Moreover, the impact of hydrostaticity on the onset of the $DyPO_4$ transition has yet to be reported. It is well-documented that higher shear components often lower P_{onset} and Lacomba-Perales *et al.* came to similar conclusions when comparing their YPO_4 findings to previous work [17, 3]. Although the effect of hydrostaticity has yet to be systematically studied for $REPO_4$s, it has been studied in other ABO_4 compounds. For example, Santamaría-Pérez *et al*. conducted a systematic study for orthorhombic $BaSO_4$ [18]. Under less hydrostatic conditions, they found that transition began earlier and that the pressure range of phase coexistence was wider. Assessing the impact of hydrostaticity on the $DyPO_4$ transition is critical as structural applications like CMCs involve a significant degree of deviatoric stress in addition to hydrostatic pressure.

This study employs *in situ* DAC synchrotron XRD to directly and quantitatively interrogate the $DyPO_4$ structure and phase behavior. To apply pressure with varying degrees of hydrostaticity, three pressure-transmitting media (PTMs) are used: neon, a 16:3:1 methanol-ethanol-water

mixture, and the soft salt KCl. Diffraction patterns are used to determine P_{onset}, calculate axial compressibilities, and develop EoS's for the xenotime and monazite phases. Our findings show a quasi-hydrostatic P_{onset} of 9.1(1) GPa – much lower than the previously reported RS-based value of 15.3(9) GPa [14]. In addition, deviatoric stresses induced by the solid PTM, KCl, trigger an even earlier $DyPO_4$ transition at least as low as 7.0 GPa. Independent of hydrostaticity (i.e., with all PTMs used here), experiments reveal a wider pressure range of xenotime-monazite coexistence than was indicated by RS, suggesting that this transition is kinetically limited. Axial data from the quasi-hydrostatic experiments show that $DyPO_4$'s response to pressure is anisotropic. 3rd order Birch-Murnaghan EoS fits yield a xenotime bulk modulus ($B_{0,X}$) of 144(1) GPa with a pressure derivative of 4 and monazite bulk modulus ($B_{0,M}$) of 180(11) GPa with a pressure derivative of 4.

II. EXPERIMENTAL DETAILS

Phase-pure xenotime $DyPO_4$ powder is obtained via precipitation reaction involving $Dy(NO_3)_3 \cdot 5H_2O$ (≥99.9% RE oxide basis, Alfa Aesar) precursor and H_3PO_4 (85% w/w aqueous solution, Alfa Aesar) and subsequent calcination. Details of these two steps are described elsewhere [[13]]. *In situ* DAC XRD is conducted at room temperature at beamline 16-ID-B, HPCAT, Advanced Photon Source, Argonne National Laboratory. For all experiments, 301 stainless steel gaskets are drilled with the HPCAT laser micro-machining system [19] and two-dimensional diffraction patterns are collected with the PILATUS 1M-F detector. The x-ray beam spot size (full width at half maximum) is approximately 4 μm (vertical) by 6 μm (horizontal). These experiments are conducted over two synchrotron beam trips, resulting in slight differences in experimental details (such as beam wavelength). These details as well as experimental details of the DACs used are listed in Table I.

TABLE I. Experimental details for each of the three PTM experiments.

PTM	Beam λ (Å)	No. Scans	Exposure time [s]	Loading rate (MPa/s)	Pressure marker	Gasket hole thickness, diameter (μm)	Culet diameter (μm)	DAC type	P_{max} (GPa)
Neon	0.48595	74	1	1.8	gold powder	~40, ~110	250	symmetric	14.8
Mixture	0.40663	26	5	1.1	ruby chips	110, 250	500	Almax easyLab plate	14.2
KCl	0.40663	16	7.5	1.6	ruby chips	68, 180	380	Almax easyLab plate	12.6

Diamond anvil cell preparation involves loading the $DyPO_4$ powder sample and the pressure marker (Au or ruby) into the gasket chamber. Great care is taken that the sample does not bridge the anvils or gasket walls for best hydrostatic conditions. Three different PTMs are used: neon, 16:3:1 methanol-ethanol-water mixture, and KCl. The 16:3:1 methanol-ethanol-water mixture is hereafter referred to as the "mixture." In the case of KCl and the mixture, after a ruby is added to the sample, the PTM is added and the cell is closed and sealed. In the neon experiment, neon gas is loaded using the GSECARS gas membrane loading system [20]. The cell is then set up with a dual membrane system for (de)compression rate control [21]. Adding the can assembly for membrane compression to the already gas-loaded cell resulted in an inadvertent initial pressure jump to ~4 GPa prior to placing the cell on the beamline. There are no reported $DyPO_4$ phase transitions below ~4 GPa (as corroborated by our mixture and KCl experiments); therefore, the initial jump in the neon experiment does not preclude any material insight. The beamline's PACE 5000 pressure controlling system is then used to pressurize the cell during the experiment [21]. Pressure is determined from the unit cell volume and 3rd order Birch-Murnaghan EoS of gold (>99.96% metals basis, Alfa Aesar) [22,23].

The mixture and KCl PTM experiments use an Almax easyLab plateDAC (Almax easyLab Inc., Cambridge, MA) and ruby chips (Almax easyLab Inc., Cambridge, MA) as pressure markers. The cell is pressurized by manual crank and pressure is determined using ruby R1 fluorescence [24]. Other distinct experiment parameters are shown in Table I. Pressures derived from ruby fluorescence are presented without error estimates as only nominal values are recorded. Although these two experiments use a different pressure marker than the neon experiment, any systematic error in pressure scales is likely minimal as the gold EoS used in this study was calibrated against the ruby fluorescence method [22]. In addition, the ruby scale used in this study was also used in Musselman *et al.*'s Raman study – ensuring pressure scale consistency with prior Raman work [14].

XRD pattern integration, masking, and background subtraction are performed using Dioptas [25]. Pattern fitting is then performed using X'Pert HighScore Plus [26]. This software fits monazite using the $P2_1/c$ cell setting as a default. Although both the $P2_1/c$ and $P2_1/n$ cell settings are valid descriptions of monazite (space group No. 14), fitted lattice parameters are converted to the $P2_1/n$ cell setting for ease of comparison to literature. The atmospheric-pressure volume of xenotime $DyPO_4$ is calculated from a synchrotron scan (λ = 0.48595 Å) at 0 GPa (prior to any

compression) using a plate DAC with no PTM. $DyPO_4$'s zero-pressure bulk modulus (B_0) and its pressure derivative (B_0') are determined by fitting volume vs. pressure data to the 3rd order Birch Murnaghan EoS with the EoSFit7-GUI program [27]. Xenotime EoS and axial compressibility fits use scans with $P < P_{onset}$, while monazite EoS and axial compressibility fits use scans with $P \geq P_{onset}$. For all other computation involving derived data (e.g., unit cell volume, gold-based pressure, cell setting conversion), Python is used to propagate error and a covariance of 0 is assumed.

III. RESULTS

All three experiments have similar quasi-static loading rates (see Table I, Fig. S1) despite the varying mode of pressure application [28]. Thus, we do not attribute differences among datasets to kinetic effects. The LeBail fitting approach is used instead of traditional Rietveld structure refinement to accommodate the significant preferred orientation present in all scans of all experiments (Fig. S2 illustrates a representative example) [28,29]. Preferred orientation appears (see Fig. S2) due to the small spot size of the beam with respect to the grain sizes of the present sample (sampling a finite number of grains) [28]. It is thus also observed for the neon loading despite the neon's better hydrostaticity. The xenotime, monazite, neon, and KCl structures used for pattern fitting were determined by Milligan *et al.*, Heuser *et al.*, Hemley *et al.*, and Froyen *et al.*, respectively [30,16,32,34].

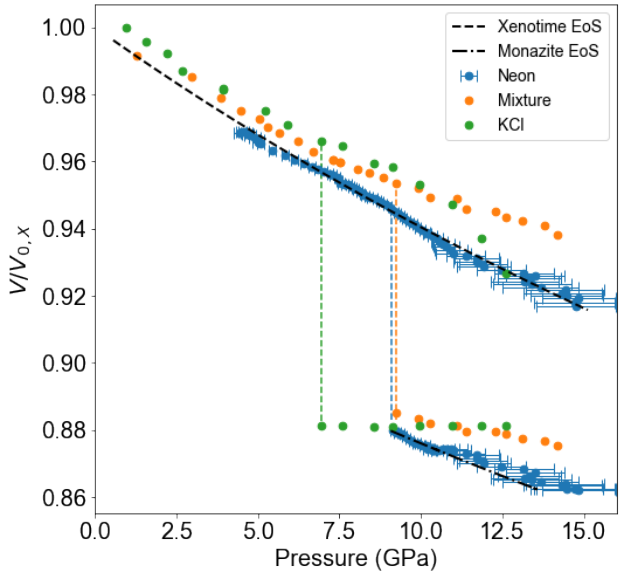

FIG. 2. (Color online) $DyPO_4$ unit cell contraction during compression under neon, mixture, and KCl PTMs. Volumes are normalized by the xenotime volume at 0 GPa, $V_{0,X}$ (in which 'X' denotes 'xenotime'). Vertical dashed lines indicate P_{onset}. For each PTM, the cluster at the top of the dashed line represents xenotime while the cluster at the

bottom of the dashed line represents monazite. Error bars represent standard deviation. In mixture and KCl datasets, pressure was recorded as a nominal value. Volume error bars for all datasets are within the symbols. Black dashed curves represent EoS fits of neon data performed with a fixed bulk modulus pressure derivative (see Table II).

The zero-pressure xenotime unit cell volume ($V_{0,X}$) used for normalization in Fig. 2 is 289.39(2) Å^3. The dashed lines show $DyPO_4$ P_{onset} values of 9.1(1) GPa, 9.3 GPa, and 7.0 GPa when pressurized with the neon, mixture, and KCl PTMs, respectively. The respective $DyPO_4$ volume contractions at P_{onset} are 6.96(3) %, 7.17(3) %, and 8.75(3) %. Figs. 3, 4, and 5 show that all XRD peaks drift to higher Q and become more diffuse due to uniform and non-uniform strain, respectively. Transformation onset is determined by visual inspection of individual XRD patterns (see Fig. S3), not by judging color in the following contour plots (Figs. 3a, 4a, and 5a) [28]. Visual inspection involves plotting the square root of intensity against Q to ensure that emerging peaks are not overlooked due to their extremely low intensity. Any given pattern is fit with both the xenotime and monazite phases only when visual inspection of that pattern reveals intensity at Q values consistent with monazite peaks. In the neon experiment, the (110), (002), and $(02\overline{1})$ monazite peaks are used to mark P_{onset} as they are the first monazite peaks to emerge and do not overlap with xenotime signal. In the mixture and KCl experiments, the (002) peak does not appear because of variation in preferred orientation between experiments. Therefore, only the (110) and $(02\overline{1})$ monazite peaks are used to mark P_{onset} in these experiments as shown in Figs. S3(b) and S3(c). All expected xenotime peaks appear in low-pressure patterns and persist after P_{onset} for all experiments. In addition, all major monazite peaks are observed at high pressure. Minor monazite peaks at $Q > 3$ Å^{-1} are more difficult to verify as they often overlap with each other or stronger PTM, pressure marker, or xenotime peaks.

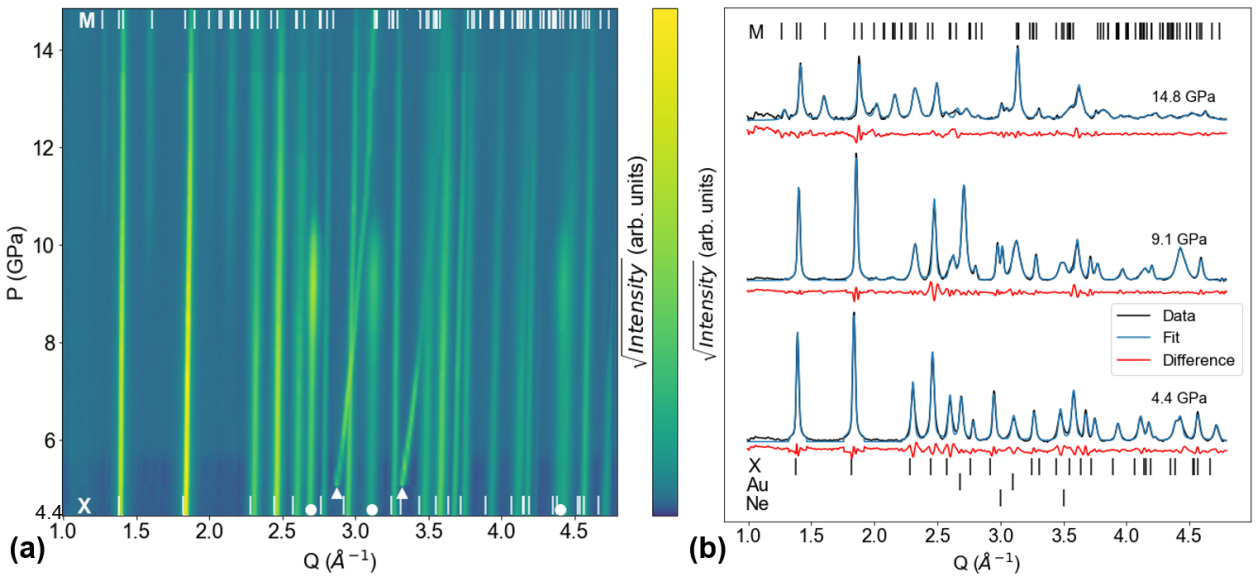

FIG. 3. (Color online) Neon dataset. 'X' ticks show a low-pressure xenotime reference pattern [30], while the 'M' ticks show a monazite fit. (a) Contour plot showing all XRD patterns. Monazite peaks emerge at 9.1(1) GPa. Circles and triangles denote the gold and neon peaks, respectively. (b) Select XRD patterns (initial, transition onset, final) and their LeBail fits.

Figs. 3(a) and 3(b) show XRD pattern evolution and LeBail fit quality (at $P_{initial}$, P_{onset}, and P_{final}), respectively, in the neon experiment. The first scan in this experiment is at a modestly high pressure of 4.4 GPa due to the gas membrane can setup and features xenotime and gold (circles in Fig. 3(a)) peaks. Non-xenotime peaks first emerge at 5.0 GPa; this corresponds to the crystallization of neon as reported in in the literature [31]. This is noteworthy as the conditions shift from hydrostatic (in liquid Ne) to quasi-hydrostatic (in solid Ne) at this point in pressure. Neon peaks shift more dramatically than the other materials' peaks because neon is the most compressible material in the DAC [32]. The first discernible monazite peaks emerge at 9.1(1) GPa and are located at Q = 1.59 Å^{-1}, 2.02 Å^{-1}, and 2.14 Å^{-1}; these are the (110), (002), and (02 $\overline{1}$) reflections, respectively. In the P_{onset} scan, the refined monazite lattice parameters are a = 6.150(1) Å, b = 6.627(1) Å, c = 6.384(1) Å, and β = 99.60(1) °. Note that around 10 GPa, the gold signal becomes extremely weak, likely due to gold grains shifting out of the beam spot following the onset of the xenotime to monazite transition. In addition, the weak gold peaks start to overlap with stronger xenotime and now-solidified neon peaks. This overlap makes precisely locating the gold peak much more difficult. As a result, the uncertainty in the fitted gold lattice parameter increases

dramatically. Since pressure is determined as a function of gold lattice parameter, the pressure uncertainty also increases dramatically.

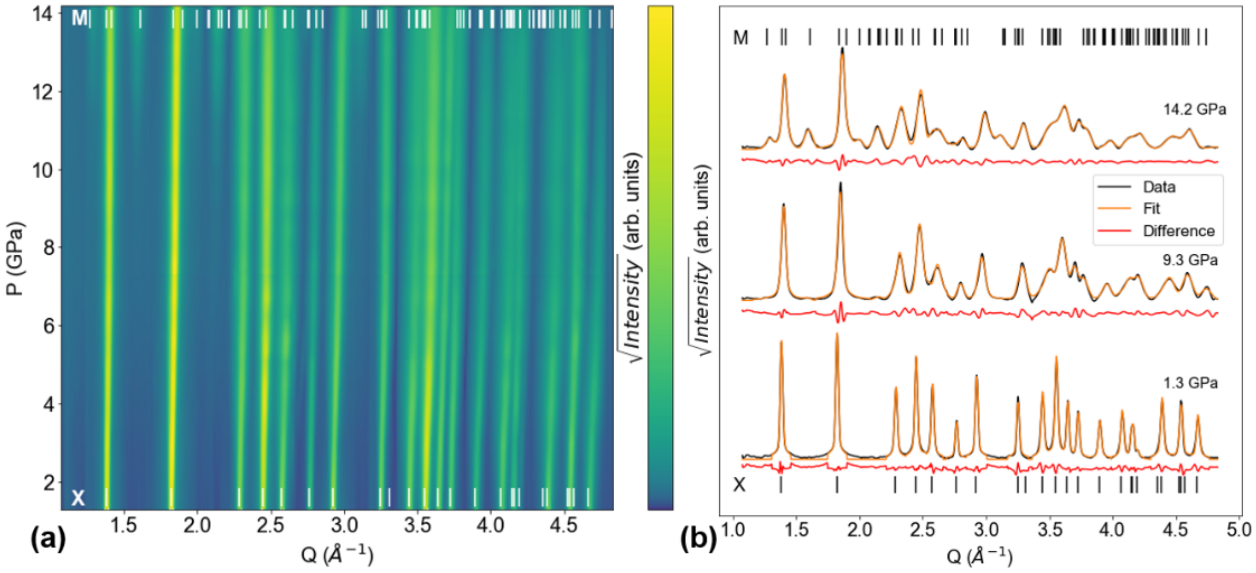

FIG. 4. (Color online) Mixture dataset. 'X' ticks show a low-pressure xenotime reference pattern [30], while the 'M' ticks show a monazite fit. (a) Contour plot showing all XRD patterns in ramp. Monazite peaks emerge at 9.3 GPa. (b) Select XRD patterns (initial, transition onset, final) and their LeBail fits.

Figs. 4(a) and 4(b) show XRD pattern evolution and LeBail fit quality (at $P_{initial}$, P_{onset}, and P_{final}), respectively, in the mixture experiment. The first scan at 1.3 GPa only shows xenotime peaks as the mixture PTM remains a liquid at this pressure and is indiscernible. The first discernible monazite peaks emerge at 9.3 GPa; these are located at Q = 1.59 Å^{-1} and 2.13 Å^{-1} and correspond to the (110), and $(02\overline{1})$ reflections, respectively. In the P_{onset} scan, the refined monazite lattice parameters are a = 6.159(1) Å, b = 6.611(1) Å, c = 6.425(1) Å, and β = 99.50(1) °. It is noteworthy that this transition commences prior to the freezing of the mixture; this means the mixture remains hydrostatic at P_{onset}. At ~10.5 GPa (the mixture's effective hydrostatic limit), the mixture undergoes a glass transition into an amorphous solid phase that contributes no XRD peaks [33].

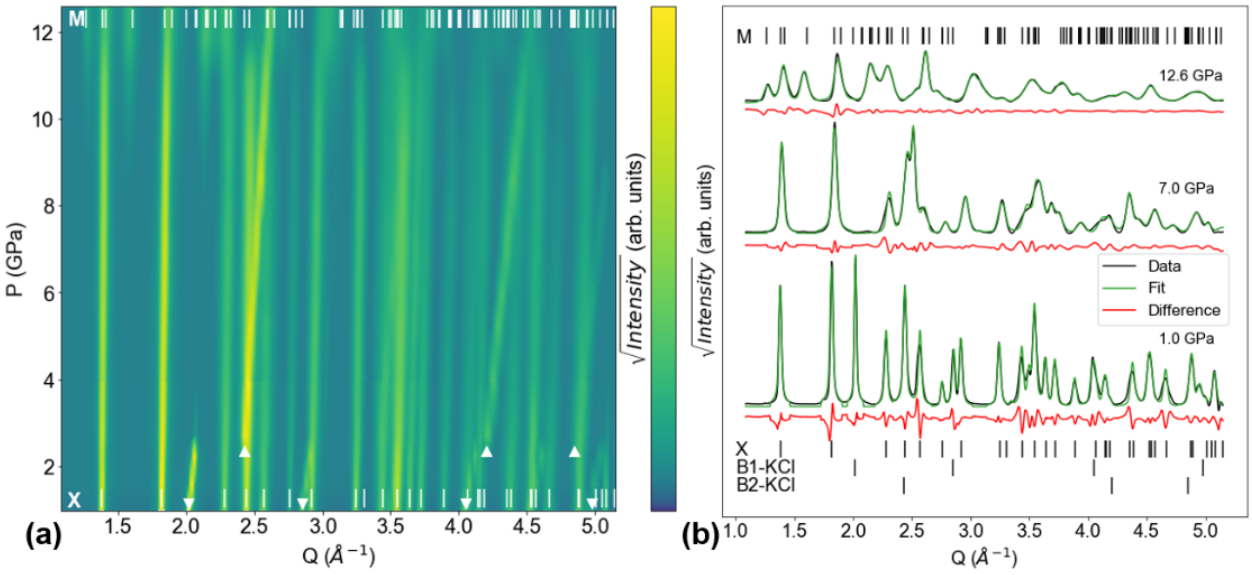

FIG. 5. (Color online) KCl dataset. 'X' ticks show a low-pressure xenotime reference pattern [30], while the 'M' ticks show a monazite fit. (a) Contour plot showing all XRD patterns in ramp. Inverted and upright triangles represent the B1 and B2 phases of KCl, respectively. Monazite peaks emerge at 7.0 GPa. (b) Select XRD patterns (initial, transition onset, final) and their LeBail fits.

Figs. 5(a) and 5(b) show XRD pattern evolution and LeBail fit quality (at $P_{initial}$, P_{onset}, and P_{final}), respectively, in the KCl experiment. The first scan shows peaks from xenotime $DyPO_4$ and B1-KCl (inverted triangles), which takes on a NaCl-type structure. At ~2.7 GPa, B1-KCl transitions to B2-KCl (upright triangles), taking on a CsCl-type structure [34]. The KCl transition does not seem to affect the phase behavior of $DyPO_4$ in the KCl transition regime. Both sets of KCl phases' peaks have higher slope than $DyPO_4$'s peaks because both KCl phases are more compressible than $DyPO_4$ [34]. In marked contrast to the neon and mixture experiments, the first discernible monazite peaks emerge early at 7.0 GPa and are located at Q = 1.58 $Å^{-1}$ and 2.12 $Å^{-1}$; these are the (110) and $(02\overline{1})$ reflections, respectively. In the P_{onset} scan, the monazite lattice parameters are a = 6.165(1), Å, b = 6.6673(5) Å, c = 6.407(1) Å, and β = 101.842(3) °. Although these uncertainties appear quite small, several checks on the LeBail fits did not change the outcome.

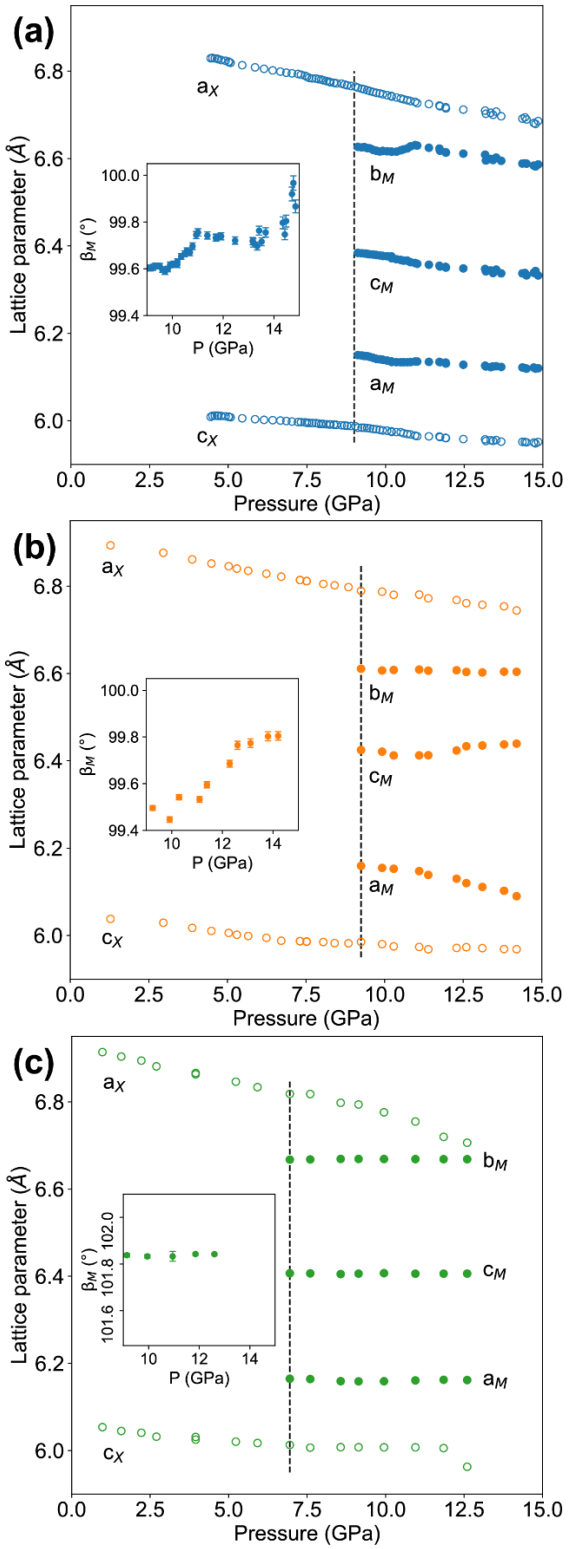

FIG. 6. (Color online) Pressure dependence of xenotime and monazite lattice parameters from the (a) neon, (b) mixture, and (c) KCl datasets. Dashed lines indicate P_{onset}. Lattice parameter error bars are within the symbol size. Insets show the monazite beta angle with standard deviation error bars. Across PTMs, consistent y-axis ranges for the panels and for the insets enable slope comparison.

Figure 6 plots the $DyPO_4$ lattice parameters from the LeBail fits for all three PTMs. Xenotime lattice parameters (a_x and c_x) steadily decrease during loading and have no apparent discontinuity or change in slope at P_{onset} across all PTMs. Monazite lattice parameters (a_M, b_M, c_M, and β_M) are less sensitive to pressure than xenotime parameters and the differences among the values of a_M, b_M, c_M are roughly the same across PTMs. β_M (shown in Fig. 6 insets) spans similar ranges in the neon and mixture datasets but spans a much higher and tighter range in the KCl dataset. Contrary to xenotime trends, monazite lattice parameter trends have some slight but statistically significant irregularities. Soon after P_{onset} in the neon dataset (Fig. 6(a)), a_M and b_M experience temporary dips and β_M experiences a temporary bump. After ~10 GPa in the mixture dataset (Fig. 6(b)), the a_M trend becomes steeper and the b_M and c_M trends become non-monotonic. It is also notable that the monazite unit cell volume does not contract upon compression in the KCl dataset – consistent with a high shear component present in the experiment.

IV. DISCUSSION

This study clearly shows that $DyPO_4$ transitions directly from the xenotime (tetragonal, $I4_1/amd$) to the monazite (monoclinic, $P2_1/n$) polymorph with no intermediate phase regardless of PTM. This result differentiates $DyPO_4$ from neighboring $REPO_4$ compositions (e.g., $TbPO_4$ and $Gd_xDy_{1-x}PO_4$), which exhibit an intermediate anhydrite phase [4]. No errant XRD peaks are observed in this study and forcing an anhydrite phase into the LeBail fits worsens fit quality. Moreover, Hay *et al.*'s revised Bastide stability diagram shows that $DyPO_4$ is too far from the xenotime-anhydrite-monazite triple point [4]. Once the monazite polymorph commences nucleation, there is a notably large pressure range of xenotime-monazite coexistence for all PTMs. In fact, the upper limit of the pressure range of coexistence remains unknown as the xenotime signal is still present in the final (highest pressure) scans taken herein. Phase fraction estimates from Rietveld refinements (see Fig. S6) show that KCl promotes more significant monazite formation than neon and the mixture in addition to lowering the onset pressure, providing evidence that shear lowers the barrier to phase transition or otherwise increases the transformation kinetics in this system [28]. Santamaría-Pérez *et al.*'s $BaSO_4$ study showed a wider coexistence range under less hydrostatic media [18], though different mechanisms and different transformation kinetics are expected in barite. Other $REPO_4$ compositions are also reported to have significant ranges of phase

coexistence [3,10]. This coexistence, however, violates Gibb's phase rule [35]. For a single-component system in which temperature is fixed and pressure is the only degree of freedom, only one phase is thermodynamically allowed to exist; therefore, the observation of a significant xenotime-monazite coexistence range even under hydrostatic conditions in this study and others suggests that the transition is kinetically limited. It would be interesting to consider future studies with variable ramp rate and at elevated temperature, but this is outside the scope of the current work.

Another significant finding is that the XRD-based P_{onset} of 9.1(1) GPa is far lower than RS-based values of 15.3(9) reported by a subset of the authors of this work [14] and 13 GPa reported by Stavrou *et al.* [15]. The large difference between RS- and XRD-based P_{onset} values is unexpected as the RS-XRD discrepancy in $TbPO_4$ (an adjacent composition) is just 0.3 GPa [9,10]. Taking a closer look at Musselman *et al.*'s Raman spectra provides a likely explanation for this 6.2 GPa gap. In that study, P_{onset} is marked by the appearance of small, distinct Raman bands representing almost all of monazite's optical modes. These modes harden with increasing pressure. Extrapolating monazite mode linear fits to lower pressures reveals that most of these modes fall within the broad peaks of xenotime modes at ~9 GPa (see Fig. S4) [28]. In other words, monazite Raman modes may exist in the ~9 GPa spectrum as weak shoulders or weak tails of xenotime Raman modes, but the poor signal-to-noise ratio of RS prevents unambiguous interpretation of these weak features as monazite signal. Stavrou *et al.*'s high pressure RS study of $DyPO_4$ reports a xenotime-monazite P_{onset} of 13 GPa [15] and presumably suffers from the same peak overlap; however, the underlying Raman spectra have yet to be published. Thus, RS is insufficient for the conclusive determination of transition onset in $DyPO_4$. Consequently, the P_{onset} of $DyPO_4$ can be revised down to this study's XRD-based value of 9.1(1) GPa. Such a revision is likely not necessary for other xenotime $REPO_4$s as they already have XRD-based P_{onset} values reported in literature [9-13]. The revised $DyPO_4$ P_{onset} also marks a significant deviation from the linear dependence of P_{onset} on RE ionic radius that is suggested in literature [4,36]. This deviation opens the intriguing possibility that at some critical ionic radius (between those of Y^{3+} and Dy^{3+}), P_{onset} has a discontinuity – i.e., it drops from above 15 GPa to below 10 GPa.

Beyond determining P_{onset} for $DyPO_4$, we find that P_{onset} is considerably stress-state dependent, with non-hydrostaticity promoting earlier transition. Neon and the mixture yield similar P_{onset} values: 9.1(1) GPa and 9.3 GPa, respectively. The latter value can be safely understood as

hydrostatic because it is lower than the mixture's hydrostatic limit (i.e., below its freezing point). The P_{onset} difference between these two experiments is marginal and may be due to the fact that they use different methods of pressure determination (the former via gold diffraction, the latter via ruby fluorescence). In contrast, the KCl experiment yields a P_{onset} of 7.0 GPa – a significant drop of ~22%. This pressure may be even lower if the ruby pressure readings are systematically overestimated due to the non-hydrostaticity of the KCl PTM. Unlike the other PTMs, KCl is a crystalline solid at all pressures and induces non-negligible shear stresses on $DyPO_4$. This is relevant for $REPO_4$s as shown by Lacomba-Perales *et al.* who report that less hydrostatic conditions result in earlier transition in YPO_4 [3] and by Heffernan *et al.* who report interesting shear-induced behaviors in $GdPO_4$ [8]. Non-hydrostaticity promoting earlier $DyPO_4$ transition is also consistent with Santamaría-Pérez *et al.*'s work on orthorhombic $BaSO_4$ and gives additional insight into the mechanism of the shear-induced lowering of P_{onset} as discussed later [18].

When evaluating lattice parameters in this study, it is critical to note that those of monazite are less accurate than those of xenotime – especially at pressures close to P_{onset} when the monazite signal is extremely weak. Weak monazite peaks located close to other weak monazite peaks or strong xenotime peaks can easily lead to improper LeBail fitting and introduce inaccuracy. Even in the final (highest pressure) scans of each experiment, the strongest monazite peak is weaker than the strongest xenotime peak. Despite this uncertainty, Fig. 6 shows that across all three experiments, the monazite lattice parameters a_M, b_M, and c_M at P_{onset} are consistent. The KCl experiment's β_M angle, however, is ~2.5° higher than that of neon and the mixture (which are in close agreement).

Furthermore, the lattice parameter trends seen in the monazite phase (see Fig. 6) also exhibit some irregularities. Soon after P_{onset} in the neon experiment, a_M, b_M, and β_M trends show temporary non-monotonicity, which is attributed to inaccurate inferred pressures rather than anomalous $DyPO_4$ behavior. At this point in the experiment, the gold peaks became extremely weak and began to overlap with stronger xenotime and neon peaks (see Fig. 3(a)). Resultant inaccuracy in the gold peak position then propagates directly to the determined pressures. In the mixture dataset (Fig. 6(b)) at ~10 GPa, the a_M trend becomes steeper and the b_M and c_M trends become non-monotonic. These irregularities coincide with the non-hydrostatic limit (10.5(5) GPa), at which point the mixture undergoes a glass transition. The KCl experiment (Fig. 6(c)) shows no contraction of the monazite unit cell due to the rather non-negligible degrees of shear stress. This is typical of phase

transitions in a high shear environment where a local drop in pressure occurs as a nucleus of the low-pressure polymorph transitions to the higher density, high-pressure polymorph. Since this localized drop will cause the transition to continue elsewhere in the sample in the absence of a hydrostatic PTM, the monazite unit cell is not expected to contract until all material is transformed.

Quantitative evaluation of these lattice parameters is further made difficult by the fact that literature does not provide lattice parameters of the high-pressure $DyPO_4$ polymorph. The best comparison point presently available is López-Solano *et al.*'s *in situ* DAC diffraction study of $TbPO_4$, a neighboring composition of $DyPO_4$ [10]. Their work uses a different monoclinic cell setting than this work, thus their a_M is equivalent to our study's c_M and their c_M is equivalent to our study's a_M. This switch explains why they report $a_M > c_M$, while Fig. 6 here shows the opposite. All linear (a_X, c_X, a_M, b_M, and c_M) lattice parameters reported herein are ~1% smaller than those reported by López-Solano *et al.*, which is expected since Dy^{3+} has a smaller ionic radius than Tb^{3+} [1]. The monazite beta angle (β_M) reported herein is ~3% smaller in the neon and mixture experiments and ~1% smaller in the KCl experiment. Like $TbPO_4$, linear lattice parameters of $DyPO_4$ decrease with pressure while β_M increases under quasi-hydrostatic loading. Another important structural metric is tetragonal distortion (c_X/a_X), which is plotted against pressure in Fig. S5 [28]. The magnitude and pressure dependence of tetragonal distortion in the neon and mixture experiments is in good agreement with the $TbPO_4$ study – suggesting that xenotime $DyPO_4$ and xenotime $TbPO_4$ distort similarly under quasi-hydrostatic loading. Both of those PTMs do not yield as great of an increase in tetragonal distortion as KCl does for the same pressure range – indicating KCl distorts xenotime $DyPO_4$ the most.

A more thorough method of assessing unit cell distortion for both xenotime and monazite is evaluating axial compressibilities (summarized in Table S1) [28]. Analyzing relative values of axial compressibilities for a given phase provides insight into a material's (an)isotropic response to stress. It is important to note beforehand that xenotime axial compressibilities are more accurate than monazite ones due to signal-to-noise ratio deterioration under high pressure. Heffernan finds that xenotime axial compressibilities follow the order "[001] << [010] = [100]," while monazite axial compressibilities follow "[100] < [010] < [001]" [38]. Xenotime data from all three experiments as well as monazite data from the neon experiment match these trends. The mixture monazite data is not consistent because the b and c parameters no longer decrease monotonically past the hydrostatic limit. KCl's monazite data is inconsistent because the lattice parameters appear

pressure-independent (i.e., the a_M, b_M, and c_M axial compressibilities are virtually 0 GPa^{-1}). This also explains why the qualities of fit for KCl monazite data (also in Table S1) are extremely poor [28]. Axial compressibility fits also provide zero-pressure parameters (y-intercepts of the linear fits), which should be consistent with the 1 atm lattice parameters in the structure files used for LeBail fitting. Xenotime zero-pressure parameters are consistent in this respect, while monazite zero-pressure parameters are not. Monazite's inconsistency may be due to an insufficient pressure range of monazite data points, aforementioned pressure-induced degradation of the XRD signal, or the metastability of the monazite $DyPO_4$ structure used as a reference in this study [16].

P-V data is fit to the 3rd order Birch-Murnaghan EoS to explore the thermodynamics of the transition and permit comparison to elastic properties measured through other methods. EoS parameters are listed in Table II and plots with EoS fits are shown in Fig. S7 [28]. Two sets of fits are performed in all cases, one with B_0' fixed to 4 and one with B_0' floating between 2 and 7. Xenotime fits fix $V_{0,X}$ to 289.39(2) $Å^3$, which is derived from a pre-compression synchrotron scan. In monazite fits, fixing $V_{0,M}$ to Heuser *et al.*'s reported value of 273.630(5) $Å^3$ [16] – as well as similar values reported by others [39-41] – leads to $B_{0,M}$ being lower than $B_{0,X}$. Such a finding would be inconsistent with the axial compressibility analysis performed herein, as well as prior high pressure $REPO_4$ XRD studies reporting $B_{0,M}$ to be ~20% greater than $B_{0,X}$ in $ErPO_4$, ~28% greater in YPO_4, and ~6% greater in $TbPO_4$ [3,10]. Previously reported $DyPO_4$ $V_{0,M}$ values likely result in this inconsistency because they are based on metastable monazite $DyPO_4$ synthesized or simulated at 1 atm. Therefore, $V_{0,M}$ is made a free parameter in the monazite fits shown in Table II.

TABLE II. Bulk moduli (B_0) and their zero-pressure derivatives (B_0') calculated by fitting volume vs pressure data to the 3rd order Birch-Murnaghan EoS. The fits themselves are plotted in Fig. S7 [28]. The weighted chi square value (χ^2_w) is the measure of goodness of fit. Fits were performed by fixing B_0' to 4 or by letting it float between 2 and 7. Numbers in parentheses after a value represent the standard deviation of the last digit of the value. The xenotime V_0 values marked with an asterisk are fixed during fitting. KCl monazite fits do not converge.

Phase	PTM	B_0' = 4			$2 \leq B_0' \leq 7$			
		V_0 ($Å^3$)	B_0 (GPa)	χ^2_w	V_0 ($Å^3$)	B_0 (GPa)	B_0'	χ^2_w
Xenotime	Neon	289.39(2)*	144(1)	0.05	289.39(2)*	135(1)	7.0(1)	0.03
	Mixture	289.39(2)*	170(1)	0.03	289.39(2)*	163(6)	6.4(20)	0.03

	KCl	289.39(2) *	204(18)	154.86	289.39(2) *	209(17)	2.0(40)	152.90
Monazite	Neon	266.57(70)	180(11)	0.96	267.02(75)	163(9)	6.4(22)	0.93
	Mixture	261.45(51)	421(33)	5.60	261.71(55)	389(33)	7.0(7)	4.91
	KCl	-	-	-	-	-	-	-

For the xenotime polymorph, χ^2_w values show that the neon dataset yields qualities of fit that are similar to those of the mixture dataset and dramatically better than those of the KCl dataset (for both B_0' conditions). Among the neon- and mixture-based fits, the neon-based, fixed B_0' fit has the best quality (χ^2_w closest to 1) and yields a $B_{0,X}$ value that is comparable to values determined using other techniques. Namely, Wilkinson *et al.* report a 122-141 GPa range using values converted from nanoindentation data and Li *et al.* report 141.5 GPa using computational chemical bond theory [42,43]. Furthermore, $B_{0,X}$ = 144(1) GPa with B_0' = 4 is consistent with $REPO_4$ compositional trends. Even the floating B_0'-based $B_{0,X}$ is between the reported $B_{0,X}$ values of $TbPO_4$ and $HoPO_4$ (the left and right lanthanide neighbors of $DyPO_4$, respectively), which are 134 GPa (B_0' = 6.4) and 152 GPa (B_0' = 4.2), respectively [10,11].

In marked contrast, the mixture and KCl datasets give $B_{0,X}$ values that are far too high. On one hand, the KCl dataset's exceedingly high $B_{0,X}$ values are consistent with Lacomba-Perales *et al.*'s observations that non-hydrostatic DAC experiments on $REPO_4$s yield overestimated moduli [3]. On the other hand, the mixture dataset's high $B_{0,X}$ values cannot be explained by non-hydrostatic stress since the mixture remains hydrostatic up to ~10.5 GPa. We suggest that this inconsistency may be due to the fact that a sprinkling of Au powder was used for pressure measurement in the neon experiment, while a ruby sphere was used in the mixture and KCl experiments. While the Au powder experienced the same (quasi-)hydrostatic conditions as the sample in the neon experiment, the ruby may have become trapped between the gasket and anvil in the mixture and KCl experiments. Trapping may have led the ruby to experience higher shear, resulting in a somewhat incorrect pressure reading. This explanation may be supported by close inspection of Figs. S7(c) and S7(e), which show that the xenotime EoS fits switch from lying below the experimental data to lying above the experimental data at ~5 GPa. Considering these issues as well as the neon data's close match with literature values as discussed above, we regard the fixed B_0' fit of the neon data as most accurate.

For the monazite polymorph, the neon dataset again yields the best fits (for both B_0' conditions) as evidenced by the respective χ^2_w values being closer to 1. The mixture dataset is significantly underfit and most of its data points are located at pressures above the mixture's hydrostatic limit (see Fig. S7(d)) [28]. In the mixture experiment, a similar behavior as in the KCl experiment is expected. That is, local pressure drops during non-hydrostatic compression introduce error into the fitted EoS (which naturally includes pressures above 9.3 GPa for the high-pressure polymorph). The KCl monazite dataset (see Fig. S7(f)) does not produce any converging fits because $B_{0,M}$ becomes negative during optimization cycles [28]. Taking a step back, this dataset should not yield reasonable 3rd order Birch-Murnaghan fits as the monazite phase is not compressed under these non-hydrostatic conditions until the entire sample volume has transitioned. Among the two neon dataset-based fits, we select the fit conducted with a fixed B_0' to have a consistent B_0' condition with the selected xenotime EoS. Therefore, we report a monazite $DyPO_4$ bulk modulus of 180(11) GPa (B_0' = 4) and a zero-pressure volume of 266.57(70) Å^3. This ~25% increase from $B_{0,X}$ to $B_{0,M}$ appears consistent with the aforementioned increases in other compositions. Evaluating the value of $B_{0,M}$ itself is made difficult by the fact that no experimental comparison exists in literature – only Kowalski *et al.*'s *ab initio* quantum chemistry calculation of 127.6 GPa [44]. This simulated value is far lower than the $B_{0,M}$ values in Table II and even lower than the $B_{0,X}$ values reported here and elsewhere in literature [42,43]. As aforementioned, one would expect $B_{0,M}$ to be higher than $B_{0,X}$ for such $REPO_4$s, as indeed is observed here. Thus, Kowalski *et al.*'s value appears underestimated for reasons yet unknown.

It may be tempting to conclude that the neon-based $B_{0,M}$ values are as accurate if not more accurate than the neon-based $B_{0,X}$ values; however, this is not the case for two reasons: first, the $V_{0,M}$ of stable (not metastable) monazite $DyPO_4$ must be ascertained with further high pressure XRD experiments as this parameter has a tremendous influence on the fitted $B_{M,0}$ value. Second, even if this neon monazite data is fit using the most accurate $V_{0,M}$, $B_{M,0}$ would still be less accurate than $B_{X,0}$ due to the coexistence of xenotime and monazite phases in all scans above P_{onset}. In other words, all scans used for xenotime EoS fitting only contain xenotime, whereas all scans used for monazite EoS fitting contain both phases.

Next, we consider the mechanism of the lowered P_{onset} due to high shear in more depth. Heffernan *et al.* elucidate the role of shear in $REPO_4$s' structural response to pressure in their *in situ* DAC study of monazite $GdPO_4$. They observe an additional $GdPO_4$ Raman band appearing at

pressures above their PTM's hydrostatic limit even though XRD suggests no such transition. The authors attribute this additional mode to shear-induced PO_4 tetrahedra distortion, which exacerbates Gd-O bond distortion [8]. Such a mechanism may also be responsible for the lower transition pressure of xenotime $DyPO_4$ in a KCl environment as we see here. That is, hydrostatic pressure may compress the Dy-O cage, but KCl-induced shear may further distort Dy-O bonds (indirectly) via PO_4 tetrahedral distortion. The magnitude of this shear may be sufficient to not only distort Dy-O bonds, but to reconfigure them – thus triggering the early transition. Our observation of the β_M angle being ~2.5 ° higher in the KCl experiment than in the other experiments also points towards a possible shear-induced distortion of the monoclinic cell. Confirming this proposed mechanism will require future *in situ* DAC single crystal XRD studies. Nevertheless, it may be scientifically interesting as well as technologically important if modifying and controlling shear could lower P_{onset} even further.

Finally, our findings can inform future $REPO_4$ work and CMC fiber coating development more broadly. Given the large discrepancy between RS- and XRD-based P_{onset} values for $DyPO_4$, XRD should be considered for conclusive P_{onset} determination in $REPO_4$ solid solutions with similar Raman band overlap (e.g., $Gd_xDy_{1-x}PO_4$). All other pure xenotime $REPO_4$s – as well as $Gd_xTb_{1-x}PO_4$ and $Sm_xTb_{1-x}PO_4$ solid solutions – have already been characterized using XRD [3,10,12,13], thus their reported transition pressures stand unaltered. Furthermore, the at least 22% reduction of $DyPO_4$ P_{onset} under KCl loading suggests that xenotime $REPO_4$ fiber coating transformation may begin at lower pressures than expected in the high-shear environment of a CMC. This in turn means that transformation-based plasticity and toughening mechanisms could be activated at lower stresses in the application environment. Therefore, a candidate material's propensity for transformation should be assessed under high-shear – in addition to hydrostatic – conditions. Using shear-sensitivity as a criterion for screening $REPO_4$ candidates potentially opens up a wider range of compositions worth considering for CMC applications.

V. CONCLUSION

This experimental study provides crystallographic proof that xenotime $DyPO_4$ transitions directly to the monazite structure upon room temperature compression. Prior Raman spectroscopy indicated a transition onset pressure of 15.3 GPa [14]; however, our synchrotron XRD study shows that transition onset is much earlier, at 9.1 GPa. All lattice parameters and their pressure

dependences are consistent with the trends reported for the neighboring $TbPO_4$ composition. By employing neon, 16:3:1 methanol-ethanol-water, and KCl as PTMs, we also explore the effect of various levels of hydrostaticity on the phase behavior, finding that non-hydrostaticity reduces P_{onset} to at least as low as 7.0 GPa. Compared to the other PTMs, KCl causes the most rapid increase in the xenotime c/a ratio and yields the highest monazite β angle. These are both likely indicators of shear-induced structural distortion of the PO_4 tetrahedra, which may have triggered the early phase transition. For all PTMs, xenotime and monazite coexist for large pressure ranges, suggesting that this transition is kinetically limited. Calculated axial compressibilities reveal the anisotropy of $DyPO_4$'s response to stress and are consistent with expectations for $REPO_4$s in general. Our 3rd order Birch-Murnaghan EoS fits of (quasi-)hydrostatic data yield a xenotime bulk modulus of 144(1) GPa and a monazite bulk modulus of 180(11) GPa (both with B_0' fixed to 4). The findings presented herein provide additional insight into the pressure-induced transition in $DyPO_4$ and how this transition could be tailored to CMC fiber coating applications.

ACKNOWLEDGMENTS

The authors thank Drs. Jesse Smith and Ross Hrubiak for performing initial alignments at the beamline, Dr. Sergey Tkachev for assisting with gas-loading samples, as well as Sarah Boardman and Yachao Chen for helping perform the beamline experiments. The authors also thank Drs. Nitin Kumar and Sina Soltanmohammed, who assisted in developing the batch-processing and batch-fitting procedures for the synchrotron data. J.S. was supported by the Department of Defense (DoD) through the National Defense Science & Engineering Graduate (NDSEG) Fellowship Program. B.H. was supported by resources at the Spallation Neutron Source (SNS) and the High Flux Isotope Reactor (HFIR), DOE Office of Science User Facilities operated by the Oak Ridge National Laboratory (ORNL). This work was performed at HPCAT (Sector 16), Advanced Photon Source (APS), Argonne National Laboratory. HPCAT operations are supported by DOE-NNSA under Award No. DE-NA0001974 and DOE-BES under Award No. DE-FG02-99ER45775, with partial instrumentation funding by NSF. Use of the COMPRES-GSECARS gas loading system was supported by COMPRES under NSF Cooperative Agreement No. EAR 11-57758 and by GSECARS through NSF Grant No. EAR-1128799 and DOE Grant No. DE- FG02-94ER14466. A.P.S. is supported by DOE-BES, under Contract No. DE-AC02-06CH11357. This research was funded by the National Science Foundation (NSF) under Award No.: DMR-1352499.

[1] L.A. Boatner, Rev. Miner. Geochem. **48 (1)**, 87–121 (2002).

[2] S. Ushakov, A. Navrotsky, and L. Boatner, 103rd Annu. Meet. Am. Ceram. Soc. (ACerS), April 22-25,2001, Indianapolis, (2001).

[3] R. Lacomba-Perales, D. Errandonea, Y. Meng, and M. Bettinelli, Phys. Rev. B **81**, 064113 (2010).

[4] R. S. Hay, P. Mogilevsky, and E. Boakye, Acta materialia **61(18),** 6933-6947 (2013).

[5] P. J. Meschter, *(19) United States (12)*, **1**, (2010).

[6] R. S. Hay, E. E. Boakye, P. Mogilevsky, G. E. Fair, T. A. Parthasarathy, and J. E. Davis, J. Am. Ceram. Soc. **96**, 1586 (2013).

[7] E. Stavrou, A. Tatsi, E. Salpea, Y. C. Boulmetis, A. G. Kontos, Y. S. Raptis, and C. Raptis, J. Phys. Conf. Ser. **121**, (2008).

[8] K. M. Heffernan, N. L. Ross, E. C. Spencer, and L. A. Boatner, J. Solid State Chem. **241**, 180 (2016).

[9] A. Tatsi, E. Stavrou, Y. C. Boulmetis, A. G. Kontos, Y. S. Raptis, and C. Raptis, J. Phys. Condens. Matter **20**, (2008).

[10] J. López-Solano, P. Rodríguez-Hernández, A. Munoz, O. Gomis, D. Santamaría-Perez, D. Errandonea, F. J. Manjón, R. S. Kumar, E. Stavrou, and C. Raptis, Phys. Rev. B **81**, 144126 (2010).

[11] Gomis, O., Lavina, B., Rodríguez-Hernández, P., Muñoz, A., Errandonea, R., Errandonea, D., & Bettinelli, M. Journal of Physics Condensed Matter, **29(9)** 095401 (2017).

[12] F. X. Zhang, M. Lang, R. C. Ewing, J. Lian, Z. W. Wang, J. Hu, and L. A. Boatner, J. Solid State Chem. **181**, 2633 (2008).

[13] F. X. Zhang, J. W. Wang, M. Lang, J. M. Zhang, R. C. Ewing, and L. A. Boatner, Phys. Rev. B - Condens. Matter Mater. Phys. **80**, 184114 (2009).

[14] M. A. Musselman, T. M. Wilkinson, B. Haberl, and C. E. Packard, J. Am. Ceram. Soc. **101**, 2562 (2018).

[15] E. Stavrou, A. Tatsi, C. Raptis, I. Efthimiopoulos, K. Syassen, A. Munoz, P. Rodríguez-Hernández, J. López-Solano, and M. Hanfland, Phys. Rev. B - Condens. Matter Mater. Phys. **85**, 024117 (2012).

[16] J. M. Heuser, S. Neumeier, L. Peters, H. Schlenz, D. Bosbach, and G. Deissmann, J. Solid State Chem. **273**, 45 (2019).

[17] D. Errandonea, Y. Meng, M. Somayazulu, and D. Häusermann, Phys. B Condens. Matter **355**, 116 (2005).

[18] D. Santamaría-Pérez, L. Gracia, G. Garbarino, A. Beltrán, R. Chuliá-Jordán, O. Gomis, D. Errandonea, C. Ferrer-Roca, D. Martínez-García, and A. Segura, Phys. Rev. B - Condens. Matter Mater. Phys. **84**, 054102 (2011).

[19] R. Hrubiak, S. Sinogeikin, E. Rod, and G. Shen, Rev. Sci. Instrum. **86**, (2015).

[20] M. Rivers, V. B. Prakapenka, A. Kubo, C. Pullins, C. M. Holl, and S. D. Jacobsen, High Press. Res. **28**, 273 (2008).

[21] S. V. Sinogeikin, J. S. Smith, E. Rod, C. Lin, C. Kenney-Benson, and G. Shen, Rev. Sci. Instrum. **86**, (2015).

[22] A. Dewaele, P. Loubeyre, and M. Mezouar, Phys. Rev. B **70**, 094112 (2004).

[23] F. Birch, J. Appl. Phys. **9(4)**, 279-288 (1938).

[24] H. K. Mao, J. Xu, and P. M. Bell, J. Geophys. Res. **91**, 4673 (1986).

[25] C. Prescher and V. B. Prakapenka, High Press. Res. **35**, 223 (2015).

[26] T. Degen, M. Sadki, E. Bron, U. König, and G. Nénert, Powder Diffr. **29**, S13 (2014).

[27] J. Gonzalez-Platas, M. Alvaro, F. Nestola, R. Angel, J. Appl. Crystallogr. **49(4)**, 1377-1382 (2016).

[28] See Supplemental Material at [*URL inserted by publisher*] for Figures S1-S7 (additional XRD- and Raman-based plots) as well as Table S1 (axial compressibilities).

[29] A. Le Bail, Powder Diffr. **20(4)**, 316-326 (2005).

[30] W. O. Milligan, D. F. Mullica, G. W. Beall, and L. A. Boatner, Inorganica Chim. Acta **70**, 133 (1983).

[31] L. W. Finger, R. M. Hazen, G. Zou, H. K. Mao, and P. M. Bell, Appl. Phys. Lett. **39**, 892 (1981).

[32] R. J. Hemley, C. S. Zha, A. P. Jephcoat, H. K. Mao, L. W. Finger, and D. E. Cox, Phys. Rev. B **39**, 11820 (1989).

[33] S. Klotz, J.-C. Chervin, P. Munsch, and G. Le Marchand, J. Phys. D. Appl. Phys. **42**, 075413 (2009).

[34] S. Froyen and M. L. Cohen, J. Phys. C Solid State Phys. **19**, 2623 (1986).

[35] J. W. Gibbs, *Scientific Papers: Thermodynamics* (Dover Publications, 1961), Vol. 1.

[36] M. A. Musselman, Master's thesis, Colorado School of Mines, 2017.

[37] A. Dewaele, A. B. Belonoshko, G. Garbarino, F. Occelli, P. Bouvier, M. Hanfland, and M. Mezouar, Phys. Rev. B **85**, 214105 (2012).

[38] K. M. Heffernan, Ph.D. thesis, Virginia Tech, 2016.

[39] M. Kizilyalli and A. J. E. Welch, J. Appl. Crystallogr. **9**, 413 (1976).

[40] Y. Hikichi, T. Sasaki, S. Suzuki, K. Murayama, and M. Miyamoto, J. Am. Ceram. Soc. **71**, C-354 (1988).

[41] A. Blanca Romero, P. M. Kowalski, G. Beridze, H. Schlenz, and D. Bosbach, J. Comput. Chem. **35**, 1339 (2014).

[42] H. Li, S. Zhang, S. Zhou, and X. Cao, Inorg. Chem. **48**, 4542 (2009).

[43] T.M. Wilkinson, Ph.D. thesis, Colorado School of Mines, 2017.

[44] P. M. Kowalski and Y. Li, J. Eur. Ceram. Soc. **36**, 2093 (2016).